Far-Field Correlations Verifying Non-Hermitian Degeneracy of Optical Modes

Sunjae Gwak,[1] Jinhyeok Ryu,[1] Hyundong Kim,[1] Hyeon-Hye Yu,[1] Chil-Min Kim,[1,*] and Chang-Hwan Yi[2,†]
[1]Department of Physics and Chemistry, DGIST, Daegu 42988, Republic of Korea
[2]Center for Theoretical Physics of Complex Systems, IBS, Daejeon 34126, Republic of Korea

(Received 9 February 2022; accepted 20 July 2022; published 12 August 2022)

An experimental verification of an exceptional point (EP) in a stand-alone chaotic microcavity is a tough issue because as deformation parameters are fixed the traditional frequency analysis methods cannot be applied any more. Through numerical investigations with an asymmetric Reuleaux triangle microcavity (ARTM), we find that the eigenvalue difference of paired modes can approach near-zero regardless of nonorthogonality of the modes. In this case, for a definite verification of EPs in experiments, wave function coalescence should be confirmed. For this, we suggest the method of exploiting correlation of far-field patterns (FFPs), which is directly related to spatial mode patterns. In an ARTM, we demonstrate that the FFP correlation of paired modes can be used to confirm wave function coalescence when an eigenvalue difference approaches near zero.

DOI: 10.1103/PhysRevLett.129.074101

Non-Hermitian degeneracy, namely, an exceptional point (EP) [1], has attracted much attention in open quantum (wave) systems because of its rich and interesting physical properties. An EP is closely related to intriguing phenomena like a mode transition on Riemann surfaces [2–4], nonconservative mode couplings [5,6], chiral mode formation [7], and nonorthogonal eigenfunctions [8,9]. So far, an EP has been found in diverse fields of science and technology such as atoms [10], lasers [11,12], optics [3,13–15], acoustics [16,17], and electronic circuits [18,19]. Particularly, an EP formation in optical microcavities has been studied in various platforms [20]: gain-loss modes [21,22], modes in coupled resonators [23–25], even-odd modes [7,26], internal-external modes [27], modes in concentric layered resonators [28], and resonance-assisted tunnelings [29]. Recent studies revealed that an EP-based sensor is a prospective candidate for ultra-high-resolution sensors [30]. Several successful implementations of EP-based sensors were reported in nanoparticle detection [31–34] and gyroscopes [35–38]. Most recently, it was also reported that an EP plays a crucial role in achieving coherent perfect absorption [39].

By definition, an EP is the parametric point at which (i) eigenvalues, as well as corresponding (ii) eigenvectors, coalesce simultaneously. Hence, one can confirm EPs only when the two conditions (i) and (ii) are fulfilled. However, thus far, EPs have been only approached indirectly through a frequency analysis: through tracking a branch cut by observing avoided resonance crossings in parameter space. This technique has been generally accepted in experiments when system parameters are controllable [7,12,13,26,40–46], yet, it is not applicable in stand-alone microcavities, where deformation parameters are fixed once a fabrication process is completed.

Meanwhile, it is well known that far-field patterns (FFPs) in generic chaotic microcavities are not isotropic. More notably, if a cavity does not preserve geometric symmetry at all, the modes in the cavity and their FFPs become chiral because of unbalancing between clockwise (CW) and counterclockwise (CCW) components of the coupled modes. We focus on the so-called chiral EP formed by this type of coupling [7,26] in an asymmetric Reuleaux triangle microcavity (ARTM) [47].

In this Letter, we numerically and analytically demonstrate that FFP correlations can be a decisive measure for confirming eigenfunction coalescence for chiral EPs. We first show that many mode pairs do not coalesce even when their eigenvalues are almost identical because of other nearby mode coupling contributions. In verification, we investigate the interrelation among nonorthogonalities, FFP correlations, and eigenvalue differences of period-5 paired modes as a function of the refractive index, which is a uniquely accessible parameter in experiments and is achieved by temperature control. Second, we demonstrate the general relation between mode coalescence and FFPs by numerically obtaining a large number of modes and analytically deriving a fitting relation between them.

The ARTM consists of six different circular arcs [47]. Each vertex of a triangle has two circular arcs with different radii, and an arc is tangentially connected to two neighboring arcs for C^1 continuity. For a constant radius r_0, five radii r_j, $j = 1, 2 \ldots 5$, are given as follows:

$$\frac{r_j}{r_0} = 1 + \epsilon\left[\beta_1 + \frac{\beta_2 \sin\phi_1 + \beta_3 \sin\phi_2}{\sin(\phi_1 + \phi_2)}\right],$$

where the coefficients $(\beta_1, \beta_2, \beta_3)$ for $\{r_1, r_2, r_3, r_4, r_5\}$ are $\{(1,0,0), (1,-1,0), (1,-1,1), (0,-1,1), (0,0,1)\}$.

Here, ϵ is the deformation parameter, and ϕ_1 and ϕ_2 are the angle at the two vertices. We set $\epsilon = 9.2$, $\phi_1 = 0.11\pi$, and $\phi_2 = \pi/2$. Please see Ref. [47] for more details.

We obtain fifteen pairs of optical modes localized on a period-5 classical orbit by employing the boundary element method (BEM) [48]. Assuming time-harmonic fields ($e^{-i\omega t}$, $\omega = ck$, c: speed of light, $i = \sqrt{-1}$), the optical modes computed are the solutions of the Helmholtz equation, $-\nabla^2\psi = n^2k^2\psi$, obeying the boundary condition of the transverse electric (TE)-polarized modes at the cavity boundary. Under the Sommerfeld radiation condition [49], the modes are decaying states described by complex-valued wave numbers $k \in \mathbb{C}$. n is the refractive index set to 1 for the outside of the cavity, while it varies around 3.3 inside the cavity. We use a dimensionless wave number kR with an average radius R of ARTM. To obtain FFPs, we compute $|\psi(\vec{r})|$ using BEM at $|r| = 50R$, where the angular distribution does not change effectively.

Figure 1(a) exemplifies one of the fifteen pairs of modes. The CW emissions are marked by f_1 (−15°) and f_3 (75°) while CCW emissions by f_2 (25°) and f_4 (−75°). The broad backward emission in the range [90°, 270°] shows mixed directions. We compare the chiralities of the modes deduced from the Husimi functions [50] (α_H) and FFPs (α_F), defined as follows:

$$\alpha_H \equiv 1 - \frac{\min\left(\int_{p<0}\mathcal{H}(q,p)dqdp, \int_{p>0}\mathcal{H}(q,p)dqdp\right)}{\max\left(\int_{p<0}\mathcal{H}(q,p)dqdp, \int_{p>0}\mathcal{H}(q,p)dqdp\right)}, \quad (1)$$

$$\alpha_F \equiv 1 - \frac{\min\left(\int_{CCW} Id\theta, \int_{CW} Id\theta\right)}{\max\left(\int_{CCW} Id\theta, \int_{CW} Id\theta\right)}. \quad (2)$$

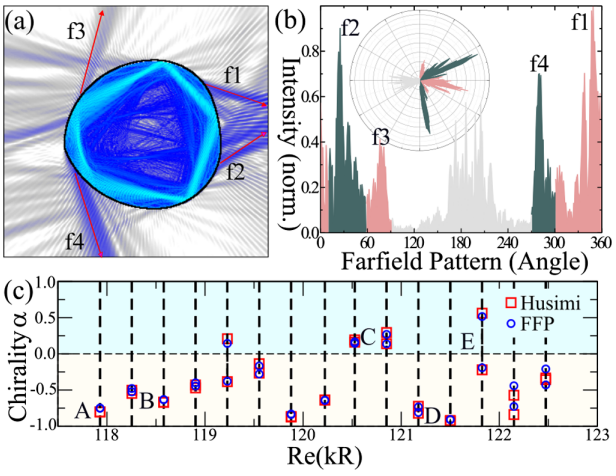

FIG. 1. (a) Wave function of mode ($kR = 121.8254 - i7.2056 \times 10^{-4}$) localized on the period-5 classical orbit. (b) FFP of the mode. The inset is FFP in the polar coordinate. The emission robes $\{f_2, f_4\}$ ($\{f_1, f3\}$) correspond to the CW (CCW) direction. (c) The chiralities versus Re(kR) of fifteen pairs of modes localized on the period-5 classical orbit.

Here, $\mathcal{H}(q,p)$ is the Husimi function obtained in the Birkhoff phase space (q,p) [51], where q is the arc length and $p = \sin\chi$ the momentum for the incident angle χ of ray. $\mathcal{H}(q,p)$ in $p > 0$ and $p < 0$, respectively, implies the CCW and the CW components of modes. In Eq. (2), θ denotes the emission angle for which $5° < \theta < 60°$ and $270° < \theta < 300°$ correspond to the CCW emission, and $60° < \theta < 90°$ and $300° < \theta < 365°$ to the CW emission, according to Fig. 1(b).

Figure 1(c) shows chiralities versus Re(kR) of the fifteen pairs of modes in $117.92 < \mathrm{Re}(kR) < 122.48$ for $n = 3.3$. Note that the two modes in each pair are nearly degenerated, as $|\mathrm{Re}(\Delta kR)| \lesssim 10^{-4}$. The equidistant mode spacing, $|\mathrm{Re}(\Delta kR)| \sim 0.3246$, between the adjacent pairs is ascribed to localization on the period-5 classical orbit. Clearly, we can identify the mutual similarity between α_H and α_F in Fig. 1(c). Note that the (−) sign of α_H and α_F are set when the denominators are the integral of $p < 0$ or CW ones.

Next, the pairwise split $|\Delta kR|$ in complex plane is obtained for $3.299 < n_e < 3.3$ in Fig. 2(a). We select five pairs (A to E in Fig. 1) to discuss. Particularly, we focus on the six dips (I to VI), where $|\Delta kR| \lesssim 10^{-5}$. At the dips, the wave function coalescence is also quantified by computing a pairwise overlap S given as follows:

$$S \equiv \frac{\left|\int_{\Omega_c} \psi_a^*(\vec{r})\psi_b(\vec{r})d\vec{r}\right|}{\sqrt{\int_{\Omega_c}|\psi_a(\vec{r})|^2 d\vec{r}}\sqrt{\int_{\Omega_c}|\psi_b(\vec{r})|^2 d\vec{r}}}, \quad (3)$$

where ψ_a and ψ_b are the modes in the same pair, and the integral domain $\vec{r} \in \Omega_c$ is the inside of the cavity. As we can see in Fig. 2(b), S is classified into two groups; $\{G_1 : (\mathrm{I}, \mathrm{IV}, \mathrm{V}), S \to 1\}$ or $\{G_2 : (\mathrm{II}, \mathrm{III}, \mathrm{VI}), S \not\to 1\}$. The

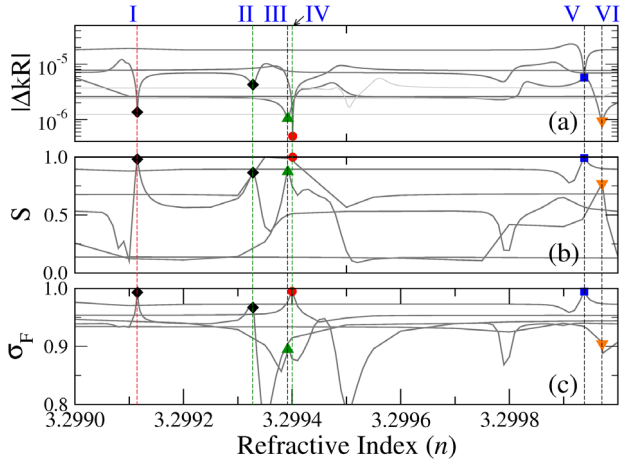

FIG. 2. Relations among (a) $|\Delta kR|$, (b) the overlap S, and (c) the far-field intensity correlation σ_F for modes obtained in $3.299 \le n \le 3.3$. (a) Six dips of $|\Delta kR|$ of selected five modes (A, B, C, D, E) in Fig. 1(c) are, respectively, marked by symbols (red circle, green triangle, black diamond, blue square, and inverted orange triangle). Corresponding peak values of S and σ_F are marked by the same symbols as well.

most peculiar finding here is that $|\Delta kR|$ and S does not hold a strict correlation. For example, comparing V and VI, we can see that $|\Delta kR|^{(\mathrm{V})} \gg |\Delta kR|^{(\mathrm{VI})}$, but, that $S^{(\mathrm{V})} > S^{(\mathrm{VI})}$. This result implies that the paired modes are "not" always collinear even when $|\Delta kR| \ll 1$, and we should examine S to confirm EPs transparently.

The observed discrepancy between S and $|\Delta kR|$ arises from other mode coupling disturbances: even when certain coupled modes are in the vicinity of their EP, if other extra modes coexist in a narrow parameter range, two-modes approximation breaks down. Then, the influence of the extra mode cannot be ignored unless we further get closer to the targeted EP in the parameter space. We demonstrate this fact by exemplifying the two cases of IV and VI shown in Fig. 2.

We consider first the case where the two-mode approximation is valid. The upper and the lower panel in Fig. 3(a) shows the weak-coupled (real-cross and imaginary-repulsion) $\mathrm{Re}(nkR)$ and $\mathrm{Im}(nkR)$ of modes corresponding to IV in Fig. 2. (Here, n is multiplied to kR to compensate the parameter variation of n.) As this pair shows $S \to 1$, the spatial distributions of the modes are almost identical as shown in the upper and the lower panel in Fig 3(b). At the same time, their $\mathcal{H}(q, p)$, exhibiting a strong localization on the CW ($\alpha_H \approx -0.986$) period-5 periodic orbit, are also almost identical as shown in the upper and the lower panel in Fig. 3(c). Consequently FFPs are also identical [Fig. 3(d)] and result in a large $|\sigma_F|$ [IV in Fig. 2]. In Figs. 3(c) and 3(g), the faint spots around the dotted line (the critical line for total-internal reflection) in $\mathcal{H}(q, p)$ are emission routes [52].

In contrast, when other extra modes couplings get involved, things change drastically. Figure 3(e) shows nkR corresponding to VI in Fig. 2. Here, we can find that the dispersion of the n-dependent trajectory of nkR is fairly distorted (see the dashed ellipse) in comparison to the above two-mode case. This distortion is caused by extra coupling between another additional mode and one of the paired modes. Because of this phenomenon known as Fermi resonance [53–56], when one of the paired modes is coupled with another mode, the spatial distribution of the mode is sure to be deformed. Thereby, the broken two-mode approximation induces nonidentical wave functions, even if $|\Delta kR|$ approaches near zero, as we can confirm in Fig. 3(f). Accordingly, all other quantities associated with EP become nonidentical either, as we can see $\mathcal{H}(q, p)$ and FFPs in Figs. 3(g) and 3(h) (also S and α_H in Fig. 2).

As observed above, measuring $|\Delta kR|$ is not enough to verify EPs because we are strictly unable to reach the exact parameter values in realistic experiments. Only approximately closer parameters are available under the experimentally allowed tolerance. Hence, to confirm EPs, examining wave function coalescence is crucial in principle. However, confirming wave function coalescence is still

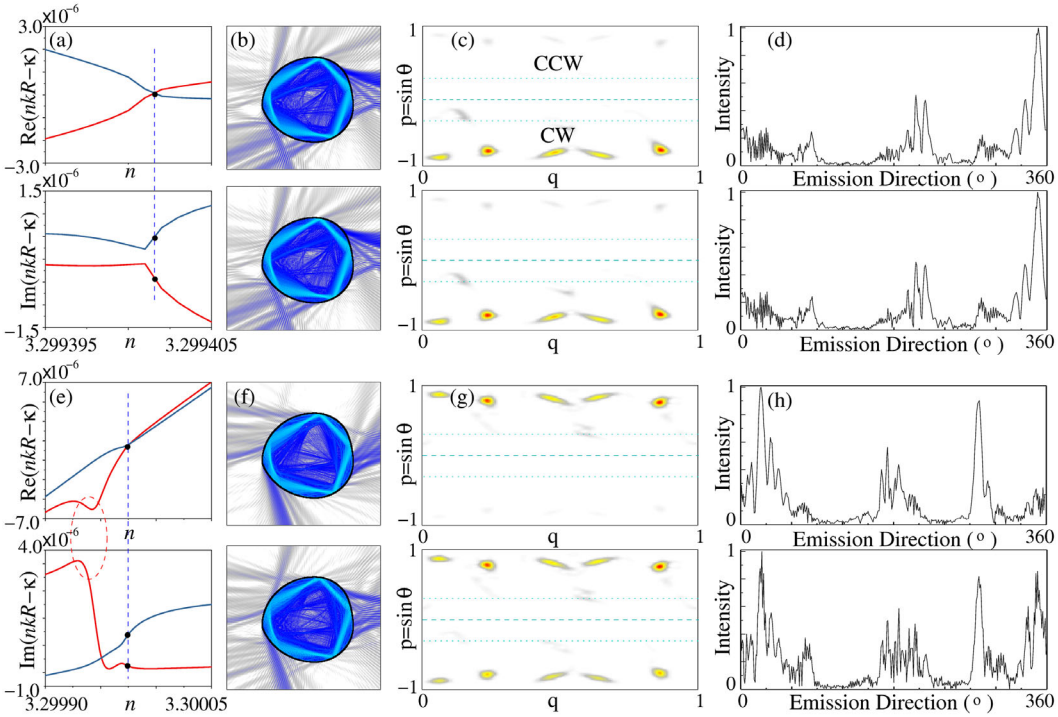

FIG. 3. (a), (e) Avoided resonance crossings of nkR as a function of n around IV and VI in Fig. 2. (b), (f) Wave function intensity in the log scale; (c), (g) Husimi functions; and (d), (h) FFPs of modes at IV and VI. In (a) and (e), nkRs are shifted as the amount of κ ($\in C$; mean nkR of the paired modes at IV and VI; dashed vertical line). In (b), (c), (d), (f), (g), and (h), the upper (lower) panels correspond to the mode having a higher (lower) $\mathrm{Im}(nkR)$ crossing the dashed vertical line in (a) and (e).

a challenging open problem, because the only available quantity is FFPs: namely, the quantity is $\propto |\psi| \in \mathbb{R}$, not $\psi \in \mathbb{C}$. Nevertheless, we can achieve this goal by utilizing the intensity cross correlation (σ_F) of FFPs. σ_F is defined as follows:

$$\sigma_F \equiv \frac{\int_{\partial\Omega_\infty} |\psi_a(\theta)||\psi_b(\theta)|d\theta}{\sqrt{\int_{\partial\Omega_\infty} |\psi_a(\theta)|^2 d\theta}\sqrt{\int_{\Omega_\infty} |\psi_b(\theta)|^2 d\theta}}, \tag{4}$$

where the integral domain $\theta \in [0 \le \partial\Omega_\infty < 2\pi]$ is a large distant measuring angle for FFPs. Note that the above intensity correlation is employed in a similar context [57]. As is shown in Fig. 2(c), the highest three values of σ_F coincide with those of S and belong to G_1. On the other hand, the lower three values of S show the lower σ_F and belong to G_2. Therefore, we can preliminarily conjecture that FFPs can be a precursor of wave function coalescence in actual experiments.

Now, we substantiate this conjecture by demonstrating that the far-field emission pattern can indeed be an indicator of wave function coalescence. We begin by constructing an effective 2×2 non-Hermitian Hamiltonian [8,9] given in terms of CW and CCW basis modes, as follows:

$$H = \begin{pmatrix} E_0 & 0 \\ 0 & E_0 \end{pmatrix} + \begin{pmatrix} \Gamma & Ve^{i\delta} \\ \eta V e^{-i\delta} & \Gamma \end{pmatrix}, \tag{5}$$

where the diagonal elements $E_0 \in \mathbb{C}$ in the first matrix stand for the degenerated basis modes ($\propto e^{\pm im\theta}/\sqrt{2\pi}$, $m \in \mathbb{Z}$) in the circular cavity. The second matrix describes a perturbation inducing an asymmetric back scattering: $V \in \mathbb{R}$ is the coupling strength and $0 \le \eta \le 1$ the real-valued asymmetricity of the couplings. $\delta \in \mathbb{R}$ is the phase of the complex-valued coupling. When $\eta \to 0$, Eq. (5) turns into the generic Jordan form [58] that results in EPs. The eigenvalues of the Hamiltonian in Eq. (5) are $E_\pm = E_0 + \Gamma \pm \sqrt{\eta}V$, and the right eigenvectors are,

$$\vec{v}_\pm = \frac{1}{\sqrt{1+\eta}}(1, \pm\sqrt{\eta}e^{-i\delta})^{\mathrm{T}}, \tag{6}$$

where we normalize the vectors to fulfill $|\vec{v}_\pm|^2 = 1$. Note that a different normalization factor $1/\sqrt{2}$ should be set [8] when we strictly use the normalization pairing of left-right eigenvectors for a non-Hermitian matrix.

To establish an explicit interconnection among the wave overlap (S), the chirality ($\alpha = 1 - \eta$) and the far-field intensity correlation (σ_F), we first obtain a large number of modes in $115 \le kR \le 125$: more than 7000 modes are obtained, as shown in Fig. 4(a). The relation between the overlap and the chirality reads

$$S = |\vec{v}_+^* \cdot \vec{v}_-| = \frac{1-\eta}{1+\eta} \Leftrightarrow \alpha = \frac{2S}{1+S}. \tag{7}$$

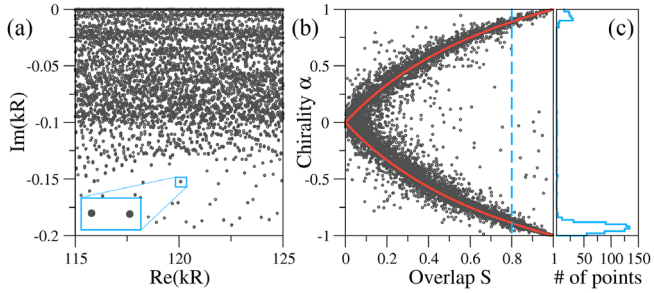

FIG. 4. (a) Wave numbers $kR \in \mathbb{C}$ of modes in ARTM. The inset enlarges one of the nearly degenerated paired modes. (b) The chirality α as a function of the wave overlap S in Eq. (7). (c) Histogram of modes having a large S (> 0.8; dashed line) that reveals CW ($\alpha < 0$)-dominant chirality.

In Fig. 4(b), we plot S-α interrelation for the modes obtained in Fig. 4(a). The analytical prediction of Eq. (7) is overlaid as solid curves. Note that the sign $+(-)$ in α is added for the CW (CCW) chirality of modes.

We now construct a relation between the far-field wave overlap $S = |\int \psi_+^* \psi_- d\theta|$ and the intensity correlation $\sigma_F = \int |\psi_+||\psi_-| d\theta$. Given the explicit expressions of normalized wave functions,

$$\psi_\pm = \frac{1}{\sqrt{2\pi}}\frac{1}{\sqrt{1+\eta}}(e^{im\theta} \pm \sqrt{\eta}e^{-i\delta}e^{-im\theta}), \tag{8}$$

we can obtain,

$$\begin{aligned}
\sigma_F &= \int_{-\pi}^{\pi} \sqrt{\psi_+^* \psi_+}\sqrt{\psi_-^* \psi_-} d\theta \\
&= \frac{1}{2\pi}\frac{1}{1+\eta}\int_{-\pi}^{\pi} \sqrt{1+\eta^2 - 2\eta\cos[2(\delta+2m\theta)]}d\theta \\
&= \frac{1}{2\pi}\frac{1-\eta}{1+\eta}\int_{-\pi}^{\pi} \sqrt{1+[4\eta/(1-\eta)^2]\sin^2(\delta+2m\theta)}d\theta \\
&= \frac{S}{4m\pi}[E(\delta+2m\pi, 1-S^{-2}) - E(\delta-2m\pi, 1-S^{-2})] \\
&\approx 1 + \frac{S-1}{2} + \mathcal{O}[(S-1)^2], \quad \text{for } S \to 1,
\end{aligned} \tag{9}$$

where $E(\phi, \xi) = \int_0^\phi \sqrt{1-\xi^2\sin^2\theta}d\theta$ is the incomplete elliptic integral of the second kind. In obtaining the expansion at the last line in Eq. (9), we utilized the commercial tool; Mathematica. With this, we now have the explicit relation $S = 2\sigma_F - 1$ in a closed form. Interestingly, it is found that the overlap S is equivalent to the multiplication of the chirality and the intensity correlation, as follows:

$$S = 2\sigma_F - 1 \Leftrightarrow S = \alpha\sigma_F. \tag{10}$$

Figure 5(b) shows that in the vicinity of EPs, i.e., $S > 0.8$, the analytic curve of Eq. (10) is well matched to the

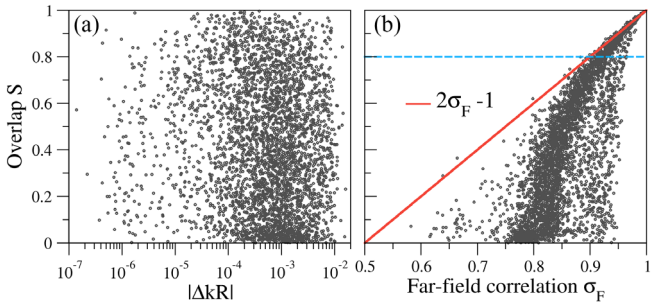

FIG. 5. The distribution of the wave overlap S versus (a) $|\Delta kR| = |k_a - k_b|R$ and (b) the far-field correlation σ_F, where (a, b) represents the paired-two modes [see, e.g., the inset in Fig. 4(a)]. S has no strong correlation with $|\Delta kR|$, while it shows a intense concentration along a nontrivial curve with σ_F. In particular, the pairs exhibiting $S > 0.8$ (dashed line) are well aligned on the curve $S = 2\sigma_F - 1$ deduced in Eq. (10).

numerically obtained (S, σ_F) distributions. Note that, employing Eq. (8), we can readily prove the relation $S = |\int_{-\pi}^{\pi} \psi_+^* \psi_- d\theta| = (1-\eta)/(1+\eta)$ in Eq. (7) as well.

In real experiments with stand-alone asymmetric microcavities and lasers, we can easily discriminate a small eigenvalue difference by using an optical heterodyne detection [59]. The beating frequency and linewidth of a mode for a probe beam correspond to the real and the imaginary eigenvalue, respectively. At the same time, FFPs can be obtained by measuring the intensities as a function of angle. Then, we can confirm wave function coalescence by exploiting FFPs.

To summarize, we find that the eigenvalue difference of paired modes can approach near zero regardless of the nonorthogonality of modes in an ARTM. For effective confirmation of wave function coalescence of chiral EPs, we propose utilizing the FFP correlation in stand-alone asymmetric microcavities. Because high-resolution experimental measurement of FFPs is feasible, we believe our findings significantly contribute to an unambiguous experimental verification of chiral EPs for their practical application to highly sensitive sensors.

This work was supported by the National Research Foundation of Korea (NRF) grant funded by the Korea government (MSIT) (No. 2021R1A2C1095623); C.-H. Y. acknowledges financial support from Institute for Basic Science (IBS-R024-D1).

C.-M. K. and C.-H. Y. contributed equally to this work as corresponding authors and S. G. and J. R. as the first authors.

*chmkim@dgist.ac.kr
†yichanghwan@ibs.re.kr

[1] W. Heiss, Phys. Rev. E **61**, 929 (2000).
[2] C. Dembowski, B. Dietz, H.-D. Gräf, H. L. Harney, A. Heine, W. D. Heiss, and A. Richter, Phys. Rev. E **69**, 056216 (2004).
[3] J. Doppler, A. A. Mailybaev, J. Böhm, U. Kuhl, A. Girschik, F. Libisch, T. J. Milburn, P. Rabl, N. Moiseyev, and S. Rotter, Nature (London) **537**, 76 (2016).
[4] Y. Choi, C. Hahn, J. W. Yoon, S. H. Song, and P. Berini, Nat. Commun. **8**, 1 (2017).
[5] H.-H. Yu, S. Gwak, H. Kim, J.-W. Ryu, C.-M. Kim, and C.-H. Yi, Opt. Express **29**, 19998 (2021).
[6] H.-H. Yu, S. Gwak, J. Ryu, H. Kim, J.-H. Kim, J.-W. Ryu, C.-M. Kim, and C.-H. Yi, Photonics Res. **10**, 1232 (2022).
[7] J. Wiersig, Phys. Rev. A **84**, 063828 (2011).
[8] J. Wiersig, S. W. Kim, and M. Hentschel, Phys. Rev. A **78**, 053809 (2008).
[9] J. Wiersig, A. Eberspächer, J.-B. Shim, J.-W. Ryu, S. Shinohara, M. Hentschel, and H. Schomerus, Phys. Rev. A **84**, 023845 (2011).
[10] H. Cartarius, J. Main, and G. Wunner, Phys. Rev. Lett. **99**, 173003 (2007).
[11] M. Liertzer, L. Ge, A. Cerjan, A. D. Stone, H. E. Türeci, and S. Rotter, Phys. Rev. Lett. **108**, 173901 (2012).
[12] S.-B. Lee, J. Yang, S. Moon, S.-Y. Lee, J.-B. Shim, S. W. Kim, J.-H. Lee, and K. An, Phys. Rev. Lett. **103**, 134101 (2009).
[13] C. Dembowski, H.-D. Gräf, H. L. Harney, A. Heine, W. D. Heiss, H. Rehfeld, and A. Richter, Phys. Rev. Lett. **86**, 787 (2001).
[14] C. Dembowski, B. Dietz, H.-D. Gräf, H. L. Harney, A. Heine, W. D. Heiss, and A. Richter, Phys. Rev. Lett. **90**, 034101 (2003).
[15] M.-A. Miri and A. Alu, Science **363** (2019).
[16] Y. Shin, H. Kwak, S. Moon, S.-B. Lee, J. Yang, and K. An, Sci. Rep. **6**, 1 (2016).
[17] W. Zhu, X. Fang, D. Li, Y. Sun, Y. Li, Y. Jing, and H. Chen, Phys. Rev. Lett. **121**, 124501 (2018).
[18] T. Stehmann, W. Heiss, and F. Scholtz, J. Phys. A **37**, 7813 (2004).
[19] Y. Choi, C. Hahn, J. W. Yoon, and S. H. Song, Nat. Commun. **9**, 1 (2018).
[20] J. Ryu, S. Gwak, J. Kim, H.-H. Yu, J.-H. Kim, J.-W. Lee, C.-H. Yi, and C.-M. Kim, Photonics Res. **7**, 1473 (2019).
[21] B. Peng, Ş. Özdemir, S. Rotter, H. Yilmaz, M. Liertzer, F. Monifi, C. Bender, F. Nori, and L. Yang, Science **346**, 328 (2014).
[22] L. Feng, Z. J. Wong, R.-M. Ma, Y. Wang, and X. Zhang, Science **346**, 972 (2014).
[23] J.-W. Ryu, S.-Y. Lee, and S. W. Kim, Phys. Rev. A **79**, 053858 (2009).
[24] S. V. Boriskina, Opt. Lett. **32**, 1557 (2007).
[25] M. Benyoucef, J.-B. Shim, J. Wiersig, and O. Schmidt, Opt. Lett. **36**, 1317 (2011).
[26] S. Gwak, H. Kim, H.-H. Yu, J. Ryu, C.-M. Kim, and C.-H. Yi, Opt. Lett. **46**, 2980 (2021).
[27] C.-H. Yi, J. Kullig, M. Hentschel, and J. Wiersig, Photonics Res. **7**, 464 (2019).
[28] J. Kullig, C.-H. Yi, M. Hentschel, and J. Wiersig, New J. Phys. **20**, 083016 (2018).
[29] C.-H. Yi, J. Kullig, and J. Wiersig, Phys. Rev. Lett. **120**, 093902 (2018).

[30] J. Wiersig, Phys. Rev. A **93**, 033809 (2016).
[31] J. Wiersig, Phys. Rev. Lett. **112**, 203901 (2014).
[32] N. Zhang, S. Liu, K. Wang, Z. Gu, M. Li, N. Yi, S. Xiao, and Q. Song, Sci. Rep. **5**, 1 (2015).
[33] W. Chen, J. Zhang, B. Peng, Ş. K. Özdemir, X. Fan, and L. Yang, Photonics Res. **6**, A23 (2018).
[34] W. Chen, Ş. K. Özdemir, G. Zhao, J. Wiersig, and L. Yang, Nature (London) **548**, 192 (2017).
[35] R. Sarma, L. Ge, J. Wiersig, and H. Cao, Phys. Rev. Lett. **114**, 053903 (2015).
[36] S. Sunada, Phys. Rev. A **96**, 033842 (2017).
[37] Y. Ren, X. Chen, Y. Cai, H. Zhang, C. Xin, and Q. Liu, IEEE Transactions on Industrial Electronics **65**, 4921 (2017).
[38] Y.-H. Lai, Y.-K. Lu, M.-G. Suh, and K. Vahala, arXiv: 1901.08217.
[39] C. Wang, W. R. Sweeney, A. D. Stone, and L. Yang, Science **373**, 1261 (2021).
[40] J. Zhu, Şahin Kaya Özdemir, L. He, and L. Yang, Opt. Express **18**, 23535 (2010).
[41] B. Peng, Şahin Kaya Özdemir, M. Liertzer, W. Chen, J. Kramer, H. Yılmaz, J. Wiersig, S. Rotter, and L. Yang, Proc. Natl. Acad. Sci. U.S.A. **113**, 6845 (2016).
[42] T. Gao, E. Estrecho, K. Bliokh, T. Liew, M. Fraser, S. Brodbeck, M. Kamp, C. Schneider, S. Höfling, Y. Yamamoto *et al.*, Nature (London) **526**, 554 (2015).
[43] J.-H. Park, A. Ndao, W. Cai, L. Hsu, A. Kodigala, T. Lepetit, Y.-H. Lo, and B. Kanté, Nat. Phys. **16**, 462 (2020).
[44] A. Bergman, R. Duggan, K. Sharma, M. Tur, A. Zadok, and A. Alù, Nat. Commun. **12**, 486 (2021).
[45] Q. Liao, C. Leblanc, J. Ren, F. Li, Y. Li, D. Solnyshkov, G. Malpuech, J. Yao, and H. Fu, Phys. Rev. Lett. **127**, 107402 (2021).
[46] H. Hodaei, A. U. Hassan, S. Wittek, H. Garcia-Gracia, R. El-Ganainy, D. N. Christodoulides, and M. Khajavikhan, Nature (London) **548**, 187 (2017).
[47] J. Ryu, J.-W. Lee, C.-H. Yi, J.-H. Kim, I.-G. Lee, H.-S. Kim, S.-B. Kim, K. R. Oh, and C.-M. Kim, Opt. Express **25**, 3381 (2017).
[48] J. Wiersig, J. Opt. A **5**, 53 (2003).
[49] S. H. Schot, Historia mathematica **19**, 385 (1992).
[50] M. Hentschel, H. Schomerus, and R. Schubert, Eur. Phys. Lett. **62**, 636 (2003).
[51] G. D. Birkhoff, Acta Math. **50**, 359 (1927).
[52] M.-W. Kim, S. Rim, C.-H. Yi, and C.-M. Kim, Opt. Express **21**, 32508 (2013).
[53] C.-H. Yi, H.-H. Yu, J.-W. Lee, and C.-M. Kim, Phys. Rev. E **91**, 042903 (2015).
[54] C.-H. Yi, J.-H. Kim, H.-H. Yu, J.-W. Lee, and C.-M. Kim, Phys. Rev. E **92**, 022916 (2015).
[55] C.-H. Yi, H.-H. Yu, and C.-M. Kim, Phys. Rev. E **93**, 012201 (2016).
[56] J.-H. Kim, J. Kim, C.-H. Yi, H.-H. Yu, J.-W. Lee, and C.-M. Kim, Phys. Rev. E **96**, 042205 (2017).
[57] S. Sunada, S. Shinohara, T. Fukushima, and T. Harayama, Phys. Rev. Lett. **116**, 203903 (2016).
[58] G. Strang, *Linear Algebra and Its Applications* (Thomson, Brooks/Cole, Belmont, CA, 2006).
[59] L. He, Ş. K. Özdemir, J. Zhu, W. Kim, and L. Yang, Nat. Nanotechnol. **6**, 428 (2011).